

Testing the Blazar Sequence with Spectra of Recently Discovered Dim Blazars from the *Fermi* Unassociated Catalog

STEPHEN KERBY¹ AND ABRAHAM D. FALCONE¹

¹*Department of Astronomy and Astrophysics
Pennsylvania State University, University Park, PA 16802, USA*

(Received 14 Mar 2024; Revised 2 May 2024; Accepted 2 May 2024)

Submitted to ApJ

ABSTRACT

Recent works have developed samples of blazars from among the *Fermi*-LAT unassociated sources via machine learning comparisons with known blazar samples. Continued analysis of these new blazars tests the predictions of the blazar sequence and enables more flux-complete samples of blazars as a population. Using *Fermi*, *Swift*, WISE, and archival radio data, we construct broadband spectral energy distributions for 106 recently identified blazars. Drawn from the unassociated 4FGL source sample, This new sample has a lower median flux than the overall sample of gamma-ray blazars. By measuring the synchrotron peak frequency, we compare our sample of new blazars with known blazars from the 4LAC catalog. We find that the bulk of the new blazars are similar to High-Synchrotron Peak (HSP) BL Lac objects, with a higher median synchrotron peak; the sample has a median $\log(\nu_{syn}/\text{Hz}) = 15.5$ via BLaST peak estimation, compared to $\log(\nu_{syn}/\text{Hz}) = 14.2$ for the 4LAC BL Lacs. Finally, we conduct synchrotron self-Compton (SSC) leptonic modeling, comparing fitted physical and phenomenological properties to brighter blazars. We find that the new blazars have smaller characteristic Lorentz factors γ_{boost} and fitted magnetic fields B , in agreement with blazar sequence predictions. The new blazars have slightly higher Compton dominance ratios than expected, which may point to alternative emission models for these dim blazars. Our results extend the predictions of the blazar sequence to a sample of dimmer blazars, confirming the broad predictions of that theory.

Keywords: active galactic nuclei — blazars; catalogs — surveys

1. INTRODUCTION

In the unified scheme of active galactic nuclei (AGN) (Blandford & Rees 1978; Urry & Padovani 1995), blazars are radio-loud AGN with a jet viewed almost directly on-axis. Electromagnetic emission from blazars is dominated by nonthermal processes producing two broad SED components; a low-energy bump (spanning from radio- to X-rays) attributed to synchrotron emission (Maraschi et al. 1992; Celotti & Ghisellini 2008) and a high-energy gamma-ray bump attributed to synchrotron self-Compton, external Compton upscattering, and/or hadronic processes like proton synchrotron and hadronic cascades (Dermer & Schlickeiser 1993; Mannheim 1993; Mücke & Protheroe 2001; Mücke et al. 2003; Celotti & Ghisellini 2008; Abdo et al. 2010a). Given their extremely broadband emission, blazars can be studied across the electromagnetic spectrum, serving as laboratories for high-energy and relativistic astrophysics in the

nearby and distant universe. Furthermore, due to their prolific high-energy emission, blazars numerically dominate catalogs of gamma-ray point sources like the *Fermi* Large Area Telescope (*Fermi*-LAT) source catalog (Abdollahi et al. 2020).

Blazars are divided into two subcategories based on the equivalent width of optical emission lines, BL Lacs having $EW < 5\text{\AA}$ and FSRQs having $EW > 5\text{\AA}$ (Stickel et al. 1991). Many blazars have high degrees of flux or spectral variability, or periodically enter flaring states; at different times, these changes make them appear alternatively as BL Lacs or FSRQs, blurring the lines between the two categories (Tavecchio et al. 1998; Abdo et al. 2010b; Bianchin et al. 2009). In general, FSRQs tend to dominate at higher redshifts and have lower synchrotron peak frequencies (ν_{syn}), while BL Lacs are more typically found at low redshift and have higher synchrotron peak frequencies. Because BL Lacs lack optical

emission lines, it is generally more difficult to constrain their redshift with spectroscopy, and many BL Lacs have unknown or highly uncertain redshift estimates. The general differences between these two subtypes and the relations between observable properties of blazars are long-running topics of current research involving more detailed study of known blazars and the expansion of catalogs with new discoveries.

The most recent release of the *Fermi*-LAT source catalog, 4FGL-DR3 (Abdollahi et al. 2022, 2020), contains 6658 sources, of which 3676 are associated with blazars. These blazars are further subdivided into BL Lacs and FSRQs, plus numerous “blazars of uncertain type” (bcu) that are likely BL Lacs and FSRQs that currently defy classification. The 4FGL catalogs represent the most complete list of gamma-ray blazars, a foundation of population studies of jetted AGN. Blazars make up a plurality of known gamma-ray sources, allowing for numerous population studies starting from high-energy observations. The blazars of the 4FGL catalog are examined in the 4LAC catalogs (Ajello et al. 2022, 2020) with spectral fitting, detailed associations, and in-depth classification.

Originating in Fossati et al. (1998) and expanded in subsequent works including Ghisellini & Tavecchio (2008) and Ghisellini et al. (2017), the blazar sequence posits an inverse relationship between gamma-ray luminosity and peak frequency of the low-energy synchrotron hump for gamma-ray blazars. Extending the predictions of the blazar sequence to even dimmer blazars suggests that the dimmest gamma-ray blazars would have even higher synchrotron peaks $\nu_{syn} > 10^{15}$ Hz. Though works like Fossati et al. (1998) and Ghisellini et al. (2017) make a physical case for the blazar sequence, the relationship between luminosity and synchrotron peak frequency has been observed for several blazar samples, regardless of any preferred physical interpretation. To this end, the continued study of gamma-ray blazars in the *Fermi* unassociated sources can test the blazar sequence by characterizing dimmer gamma-ray blazars and comparing with the bright blazars used to construct the original blazar sequences.

The blazar sequence is not entirely without controversy. As with many flux-limited samples throughout the history of astronomical research, there is a real possibility of observational biases against certain types of blazars. Some recent arguments suggest that the relationships of the blazar sequence are selection effects (Giommi et al. 2012; Giommi & Padovani 2015) leading to samples biased against dim, red blazars. For example, a dim blazar with low peak frequencies might be too dim in gamma-rays to be detected or associated in *Fermi*

catalogs, preventing the construction of a sample of red dim blazars. Blazars in the unassociated *Fermi* sources can serve as a valuable sample to test these competing hypotheses; as the unassociated sources have generally lower gamma-ray fluxes than the associated sources, the blazars of the unassociated sources could include some red dim blazars. If the dimmest blazars have a disproportionate mix of high and low ν_{syn} , the general predictions of the blazar sequence may need to be revised.

2157 of the 4FGL sources are labeled as unassociated, lacking confident association with lower-energy counterparts. These gamma-ray sources represent a treasure trove of new objects to test prominent theories of high-energy astrophysics. Given that a plurality of associated sources in 4FGL-DR3 are blazars, extrapolation suggests that there are hundreds if not thousands of blazars in the unassociated sources. If identified and investigated, these blazars can significantly supplement current catalogs of gamma-ray blazars (Ajello et al. 2022) with lower-flux blazars to combat flux biases in established samples and test the limits of current blazar theory.

Given the multiwavelength nature of blazars, gathering flux data from as wide a range of energies as possible is an important tool for analyzing blazars in a broad-band context. The blazars of the 4LAC catalog have been extensively surveyed and investigated, many having spectroscopic redshifts, but any blazars found in the unassociated source sample have much sparser coverage. As the unassociated sources often lack targeted observations, the counterparts localized to within $\sim 5''$ with *Swift* observations in (Kerby et al. 2021) make it feasible to sift through crowded optical, IR, and radio catalogs searching for spatially coincident emission. Because these counterparts are only recently characterized, in-depth population analysis of the unassociated sources is still in its nascent stages.

The position of the νF_ν peaks in the low-energy and high-energy bumps ν_{syn} and ν_{Com} plus the ratio of the fluxes at both peaks (the Compton dominance ratio) are relevant quantities that help characterize the physical processes of individual blazars. ν_{syn} constrains the typical electron energy and magnetic field within the emitting region of the blazar jet. ν_{Com} , when compared to ν_{syn} , expresses a relativistic boosting factor for upscattering of photons in an SSC model but can also constrain alternative emission models including hadronic and external Compton methods. Finally, investigating Compton dominance gives insights into specifics of the emissions processes of the jet. All three can be obtained from the SED alone without physical modeling, and indeed works like Ajello et al. (2020) obtain values for each using polynomial or log-normal fits to broadband SEDs.

Physical modeling of jet mechanics, while involving several degenerate parameters requiring in-depth observations to constrain, produces estimates both for physical jet parameters and for phenomenological variables like ν_{syn} .

In this work, we use two recently published tools to estimate these spectral properties and examine our sample of 106 blazars identified from the *Fermi* unassociated sources (the “new” blazars). **BLaST** (Glauch et al. 2022) uses machine learning trained on almost 4000 known blazar SEDs to predict the positions of the synchrotron peak frequency, being especially resilient against misreading processes like dust or disk emission as jet synchrotron emission. We apply **BLaST** to our sample to obtain one estimate for ν_{syn} . We also conduct SSC modeling of our SEDs using the **agnpy** modeling package (Nigro et al. 2022) with a **sherpa** fitting routine to estimate the physical jet parameters in each of the new blazars. While these fits have numerous degeneracies between physical parameters and fairly large uncertainties, producing reasonable fits to the SED allows for numerical location of peak frequencies and Compton dominance while comparing to the physical parameters of brighter blazars.

In section 2 we describe the sample of likely blazars identified from the unassociated *Fermi* sources, and we describe the archival data used to build broadband SEDs of each blazar. In section 3 we derive spectral properties for each blazar SED, and we conduct physical fitting of the emission mechanisms for each. Finally, in section 4 we compare our results to established catalogs of brighter blazars in the 4LAC catalog, contextualize our results with respect to current debates in blazar theory, and suggest next steps for further analysis. In this work we adopt a Λ CDM cosmology with $h = 0.7$ and $\Omega_M = 0.3$.

2. SAMPLES AND SPECTRA

2.1. The New Blazar Sample

Kerby et al. (2021) (henceforth K21) describes recent results of an ongoing campaign of *Swift*-XRT and -UVOT observations at *Fermi* unassociated sources, producing a list of over 200 such unassociated targets with X-ray and UV/optical counterparts. Neural network classification trained on established lists of gamma-ray blazars and pulsars showed that 135 of the examined sources were likely blazars, creating a sample of dim blazars with gamma-ray, X-ray, and UV/optical detections. The localization of *Fermi* unassociated sources to within $5''$ using X-ray detections, down from the $\sim 2'$ uncertainty ellipses in the *Fermi* catalog, is similarly a

vital step in further studies of the unassociated sources, allowing for detailed and precise follow-up.

Subsequently, Kaur et al. (2023) (henceforth U22) combined *Fermi* gamma-ray features, *Swift* spectral parameters, and WISE colors to classify the new blazar sample into likely BL Lac or FSRQ categories. The neural network classification in U22 suggested that the majority of our sample of new blazars were more similar to BL Lacs than FSRQs. Collected results and cross-references in U22 showed that the new blazars have properties and redshifts at first glance moderately similar to known blazars, a starting point for this more in-depth analysis of the new blazars. The 106 new blazars in U22 is the foundation of the sample used in this work, reduced from the 135 likely blazars detailed in K21 by requiring WISE IR counterparts.

Using only the *Fermi* gamma-ray data for the unassociated sources, it is possible to do a rudimentary comparison with the known blazars of the 4LAC catalog by making a few assumptions. Applying the median redshift of the BL Lacs in the 4LAC catalog (Ajello et al. 2022) $z = 0.34$ to the new blazars assumes that the new blazars have the same redshift distribution as the brighter 4LAC BL Lacs. In this way, we can estimate the gamma-ray luminosities of the new blazars if they are within the same redshift range as the 4LAC BL Lacs. The histogram in Figure 1 shows the gamma-ray luminosity of the 106 new blazars (green) assuming $z = 0.34$ compared to the 4LAC BL Lacs (blue) and FSRQs (red) with known redshifts. Since our sample of new blazars certainly has a diverse range of redshifts, we also plot two additional histograms representing the luminosity estimates if the new blazars are at the 25th and 75th percentiles of the BL Lac redshift distribution to illustrate a range of possible luminosities.

Comparing the luminosity distributions, it is clear that if the new blazars have roughly the same redshift distribution as the known BL Lacs, then they are intrinsically much lower luminosity than the 4LAC BL Lacs, and of course even dimmer still than the 4LAC FSRQs. Alternatively, if the new blazars are intrinsically the same luminosity as the known BL Lacs, they must be higher redshift. Some combination of these two effects is also feasible, with the new blazars being both higher redshift and lower luminosity. Given the results of K21 and U22, the blazars found in the unassociated source sample are dimmer than the typical BL Lac or FSRQ in the 4LAC catalog and also have properties more like BL Lacs than FSRQs. More detailed spectral analysis tests these and other findings about dim blazars.

2.2. SED Construction

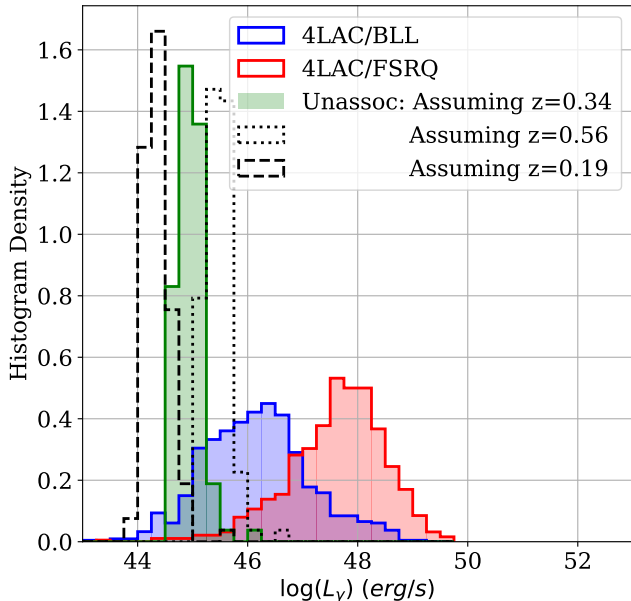


Figure 1. Comparing the gamma-ray luminosities of 4LAC BL Lacs (blue) and FSRQs (red) with estimated luminosities for the new blazars (green) assuming the same median redshift as the BL Lac sample $z = 0.34$.

The *Fermi*-LAT point source 12-year catalog (4FGL-DR3, Abdollahi et al. 2022) includes the gamma-ray fluxes for each unassociated source in eight energy bands, plus upper and lower uncertainties for each band. Given the lower average flux of the unassociated sources, many of the fluxes in individual energy bands are marginal, with lower error bars extending to zero. The units of the *Fermi* catalog νF_ν fluxes are erg/s/cm^2 , the required unit for the subsequent analysis techniques, so no conversions are necessary to begin building multiwavelength SEDs for each new blazar. For each energy band, we use the logarithmic center of the range of each energy band converted to Hz as the central point.

Building off the *Fermi* fluxes, we incorporate the *Swift*-XRT data used in K21 and U22 into each spectrum. While K21, U22, and other previous works conducted independent X-ray fitting using power-law models, for this work we use raw photon lists to facilitate physical modeling. Similarly to the *Fermi*-LAT analysis, we sum up the νF_ν flux in each of five logarithmically spaced bins between 1 and 10 keV, using Poisson statistics to infer the uncertainties on the photon flux in each bin. Assuming the galactic n_H values for each source position (Wilms et al. 2000), we rescale the XRT observed flux values to unabsorbed flux.

Though the *Swift*-XRT detector can observe photons with energies as low as 0.3 keV, we exclude the lower energy range from 0.3 to 1 keV due to the dramatic upper

and lower error bars produced by a combination of low photon statistics, high flux uncertainties, and significant n_H corrections at low energies. The large error bars proved troublesome for comparing the analysis methods detailed below, and few photons were lost by excluding this lower energy range.

Notably, because the observations used to construct SEDs for these dim blazars draw on a wide range of archival data and are not simultaneous, different energy bands could include observations with the blazar in flaring or quiescent states. Unfortunately, there is little after-the-fact recourse for the problem of non-simultaneous observations for these extremely dim blazars because the summation of over a decade of *Fermi* observations was necessary to obtain gamma-ray detection and launch our multiwavelength analysis.

Several of the *Fermi*-LAT and *Swift*-XRT energy bands have lower limits that include zero, as shown in Figure 2. The *Fermi* fluxes and errors are extracted directly from the 4FGL database, precluding rebinning. While the dimmest *Swift*-XRT counterparts have lower limits that reach zero within some specific energy bins, the energy-integrated detection procedure explained in Kerby et al. (2021) ensures that only $S/N > 4$ XRT sources are included in this work. These lower limits do not interfere with the analysis detailed below.

All the likely blazars in our sample have UV or optical detections in one or more of the six filters of the *Swift*-UVOT detector. These lower-energy counterparts are described in K21, the magnitudes already corrected for absorption. For each counterpart, the UVOT AB magnitudes are each converted to νF_ν flux via the standardized relation given in Equation 1, using the centroid frequency for each UVOT band as the ν value for placing each magnitude on the SED.

$$\nu F_\nu = \nu \times 10^{\frac{m+48.6}{-2.5}} \text{ erg/s/cm}^2 \quad (1)$$

In U22, each likely blazar had WISE magnitudes extracted via source cross-match with the WISE all-sky source catalog (Cutri et al. 2012) within the positional uncertainty of the *Swift*-XRT detection, $5''$. While U22 used WISE colors for neural network classification of likely blazars, we convert the w1, w2, and w3 magnitudes of each likely blazar to AB magnitudes using the magnitude offsets given in Table 8 of Section 4.4h on the

WISE data processing website¹. The AB magnitudes are similarly converted to fluxes via Equation 1.

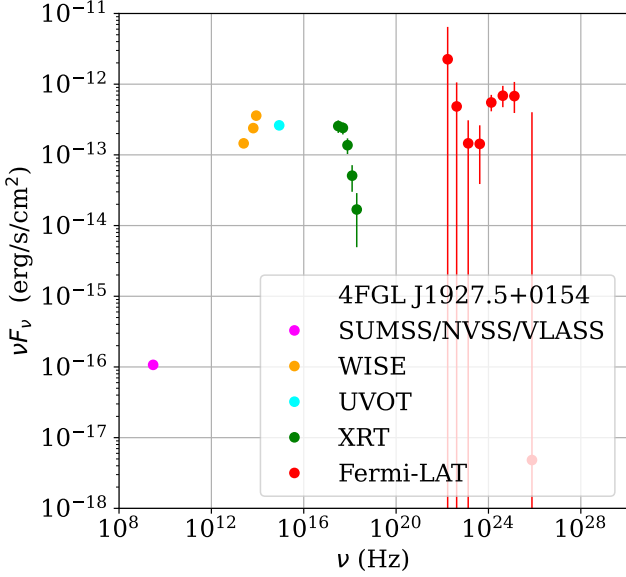


Figure 2. A typical SED for a blazar in our sample. SEDs of all of the 106 new blazars are available in an associated repository, and a small selection of characteristic SEDs is presented at the end of this paper.

WISE magnitudes are vital for constraining the low-energy side of the synchrotron peak of blazars and for demarcating the synchrotron peak frequency, as in blazars they often occupy the beginning of the power-law slope decreasing to lower energies. Especially for dim blazars, the total emission from AGN-hosting galaxies includes other components that can contribute significantly in the IR band, such as galactic stellar emission.

Finally, we conduct a position cross-match between the XRT centroids of the likely blazars with the SUMSS (Mauch et al. 2003), NVSS (Condon et al. 1998), and VLASS (Gordon et al. 2021) radio surveys. The cross-match again has a tolerance of 5'', the localization of the *Swift*-XRT detections. While these three surveys together cover the entire sky, many of the likely blazars do not have counterparts in the point source lists of these surveys. Given the steep radio slope of many blazars, it is not unexpected that dim blazars like those in our sample can be undetected in the above catalogs. Fluxes in mJy for radio counterparts are converted to νF_ν in erg/s/cm².

Combining the gamma-ray through radio fluxes, we produce a SED for each source such as that shown in

Figure 2. After examining each of the 106 likely blazars manually, all show a feasible "two hump" spectrum characteristic of a blazar, typically with radio through X-ray forming the low-energy synchrotron peak and with gamma-ray emission constraining the high-energy peak. The fact that most of the sources have negative spectral indices in the X-ray suggests that the X-ray emission is not located in the trough of the two-hump spectrum or in the high-energy peak, but instead in the synchrotron peak. This is an early indication that many of the likely blazars in our samples have high synchrotron peak frequencies, as the X-ray spectra of FSRQs with low ν_{syn} often shows positive slope on the low-energy side of the high-energy bump (Ghisellini et al. 2017).

3. SED ANALYSIS

3.1. BLAST Synchrotron Peak Estimation

The recently released BLAST tool (Glauch et al. 2022) is a machine learning estimator for predicting the νF_ν synchrotron peak frequency ν_{syn} given a multiwavelength SED for a blazar. BLAST has not yet been independently applied to new samples of blazars, so our multi-pronged approach to SED analysis allows for methodological comparisons on a unique sample. BLAST, trained on a sample of 3793 blazars with ν_{syn} ranging from 10^{12} to 10^{18} Hz, showed improvements compared to the polynomial fitting of the 4LAC-DR2 (Lott et al. 2020) values for ν_{syn} , especially in blazars with significant IR or optical excesses from non-synchrotron components like disk or dust emission.

Using the SEDs constructed in Section 2.2, we use BLAST to estimate the synchrotron peak frequency for our sample, along with the uncertainty in ν_{syn} . Given the predictions of the blazar sequence, estimating ν_{syn} can show if the dim blazars have high synchrotron peaks to extend the blazar sequence or if they have low synchrotron peaks to break from it. The results of the BLAST estimations are shown in the left panel of Figure 3.

With a median $\log(\nu_{syn}/\text{Hz}) = 15.5$, the new blazars have significantly higher synchrotron peak frequencies than the populations of BL Lacs or FSRQs in the 4LAC catalog. The BL Lacs in the 4LAC catalog have a median $\log(\nu_{syn}/\text{Hz}) = 14.2$ while the 4LAC FSRQs have a median $\log(\nu_{syn}/\text{Hz}) = 12.7$, suggesting that few if any of our new blazars are similar to FSRQs and that they tend to have rather high ν_{syn} even for BL Lacs. Figure 3 shows how distribution of ν_{syn} for the new blazars mostly overlaps with the high synchrotron-peaked BL Lacs of the 4LAC catalog.

With the BLAST estimations for ν_{syn} , it is possible to place the new blazars in the context of the blazar se-

¹ https://wise2.ipac.caltech.edu/docs/release/allsky/expsup/sec4_4h.html

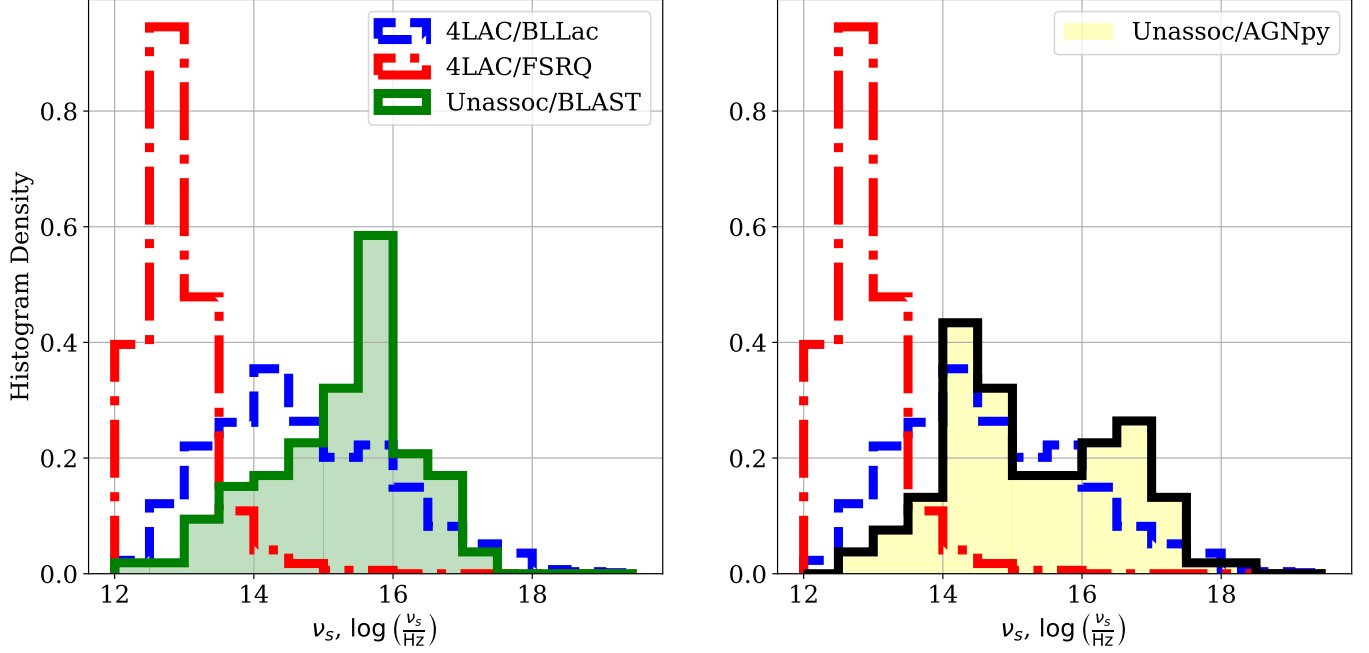


Figure 3. Synchrotron νF_ν peak frequency ν_{syn} for the new blazars via BLAST (green, left) and agnpy (yellow, right) compared to 4LAC FSRQs (red dash-dot) and BL Lacs (blue dashed). The green and yellow histograms do not show a significant population of new blazars with low ν_{syn} , in agreement with the predictions of the blazar sequence.

quence by plotting ν_{syn} versus L_γ , the gamma-ray luminosity estimated from the median redshift of the BL Lac and FSRQ 4LAC samples. In this way, we replicate Figure 2 from Finke (2013), a previous result that shows inverse relationship between synchrotron peak frequency and luminosity for BL Lac objects. Conducting this comparison also tests the prediction of U22 that the new blazars are more like BL Lac objects than FSRQs.

Figure 4 superimposes the new blazars onto the brighter BL Lacs and FSRQs from the 4LAC catalog. Applying the 25th, 50th, and 75th percentiles of redshift from the 4LAC BL Lac sample, we predict the gamma-ray luminosities of the new blazars. For the small subset of our sample of new blazars with low synchrotron peaks, we also predict their luminosities with the percentiles from the 4LAC FSRQ sample, as these blazars may be FSRQs given their ν_{syn} values.

Clearly, if the new blazars have the same redshift distribution as the known BL LACs, they represent a sample of intrinsically lower luminosity blazars, with median absolute luminosity lower by approximately an order of magnitude. Likewise, placing the new FSRQ blazars at the same distance as the typical FSRQ population, leads to the result that the new FSRQs are several orders of magnitude lower luminosity than the median 4LAC FSRQ. The lower flux observed from the new blazars could be due to physical jet parameters like a decreased Doppler factor δ_D , which in turn is determined by bulk

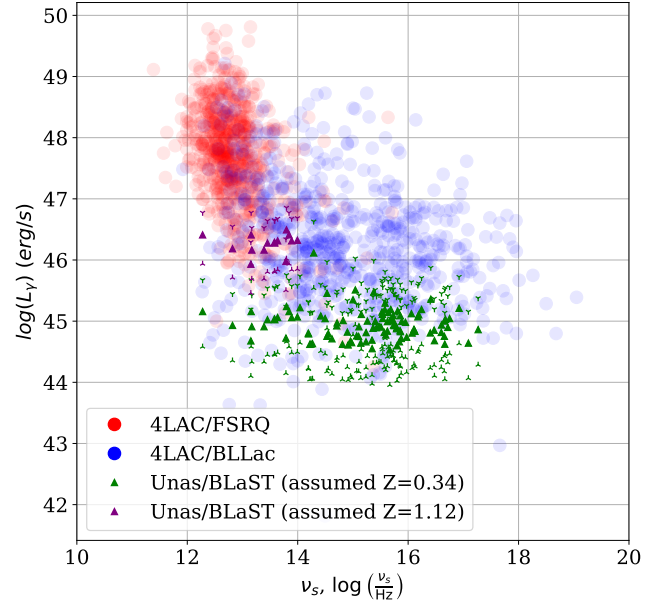


Figure 4. Synchrotron νF_ν peak frequency ν_{syn} via BLAST versus gamma-ray luminosity for the 4LAC FSRQs (red, transparent), BL Lacs (blue, transparent), and new blazars. Green points and arrows represent the new blazar luminosities using 25th, 50th, and 75th percentiles of the 4LAC BL Lac redshift distribution. Purple points represent the same, using the percentiles for the 4LAC FSRQs

Lorentz factor or viewing angle. The BLAST estimations

for ν_{syn} and its uncertainty are presented in two columns of Table 2.

3.2. *agnpy* SSC Modeling

We also apply the *agnpy* fitting package (Nigro et al. 2022) to our collection of SEDs with three aims. While BLaST produces an estimate for ν_{syn} , *agnpy* models physical parameters of the emitting jet. Secondly, *agnpy* allow us to extract phenomenological parameters like Compton dominance ratio, ν_{syn} , and high-energy peak wavelength ν_{Com} from a modeled spectrum regardless of exact physical parameters. These values allow for direct comparison with established blazars from the 4LAC catalogs, which includes many of these phenomenological parameters. Finally, we can compare the ν_{syn} predictions of BLaST and *agnpy*, as both tools are relatively new and comparisons can reveal biases or problems yet undetected in both.

To fit the blazar SEDs using *agnpy*, we use a one-zone SSC model for blazar emission, with the electrons in the jet having a broken power law γ distribution. While the combination of these models is elementary and neglects various alternative or supplementary emission mechanisms such as hadronic processes or external synchrotron upscattering, it is appropriate for first-look fitting of these dim blazars with few observations. The SSC model implemented in *agnpy* is fully described in Nigro et al. (2022) and Finke et al. (2008).

For both BLaST and *agnpy*, we included flux errors on each νF_ν data point. *agnpy* uses these one-sigma errors while fitting with the *sherpa* and *gammapy* subroutines, but BLaST seems to be unaffected by the flux estimates on individual data points. Indeed, we created a test SED and obtained numerous ν_{syn} estimates via BLaST, with unchanging results regardless of altered errors. Regardless, lower limits that include zero due to the dimness of our sample (for example, several of the *Fermi*-LAT points in Figure 2) are not impactful for ν_{syn} estimation either by being seemingly ignored (for BLaST) or as less constraining than flux bands with tighter errors (for *agnpy*).

We apply Nelder-Mead (Nelder & Mead 1965) optimization with starting parameter estimates and allowable ranges shown in Table 1. The broken power law electron distribution has six parameters: break Lorentz factor γ_b , minimum and maximum electron factors γ_{min} and γ_{max} , power law indices below and above the break p_1 and p_2 , and scaling factor k_e . The SSC model has three further parameters: magnetic field strength B , a Doppler factor $\delta_D = \frac{1}{\Gamma(1-\beta \cos \theta)}$ which depends on bulk Lorentz factor and viewing angle, and variability timescale t_{var} . Finally, the entire spectrum has a red-

shift z which we fix at $z = 0.34$, the median redshift of the 4LAC BL Lac blazars. While our sample of dim blazars certainly has a wide range of redshifts, and may have a higher median redshift to partially account for their lower flux, holding the redshift constant during fitting reduces degeneracies between parameters like t_{var} or δ_D and luminosity distance. If one should assume that a blazar in our sample has a higher redshift than the median 4LAC BL Lac, other fitted parameters like δ_D can increase monotonically to maintain the same observed flux.

For the SSC fitting, there are various degeneracies between physical jet parameters in the model, especially when fitting dim blazars that do not have substantial observations constraining redshift and magnetic field. For example, Equation 21 of Finke et al. (2008) gives the expression for synchrotron emission as

$$f_\epsilon^{syn} = \frac{\sqrt{3}\delta_D^4 \epsilon' e^3 B}{4\pi h d_L^2} \int_{-\infty}^{+\infty} d\gamma' N'_e(\gamma') R(x) \quad (2)$$

with ϵ' the energy of emitted photons in the jet frame, $N'_e(\gamma')$ the electron distribution in the jet frame, and $R(x)$ a dimensionless scaling parameter. SSC modeling uses Equation 2 to fit each SED, but the first term of Equation 2 shows a clear degeneracy between δ_D and d_L , neglecting certain second-order effects. Indeed, by holding all other variables constant and running δ_D through a range of values, the redshift z monotonically changes to create almost completely identical fits for a given blazar. By holding $z = 0.34$ for our fitting, we shift uncertainty to other parameters like δ_D .

With more detailed observations and analysis such as radio observations or by obtaining photometric/spectroscopic redshifts, δ_D or z could be independently constrained for our sample of blazars. Without those more detailed observations, it could be appropriate to compare δ_D and z to brighter blazars by combining them into a composite parameter. Because of this degeneracy and others, our analysis of the fitting results focuses on jet parameters with little degeneracy or on broadband spectral properties like Compton dominance, while more directed future observations will be necessary to exactly constrain all intrinsic properties of our sample of blazars.

Table 1. SSC parameter initialization and ranges for *agnpy* fitting.

Parameter	lower	initial	upper
-----------	-------	---------	-------

Table 1 *continued*

Table 1 (*continued*)

Parameter	lower	initial	upper
$\log(k_e)$	-12	-4	0
p_1	-2	2.5	4
p_2	1	4	8
$\log(\gamma_b)$	2	5	6
$\log(\gamma_{min})$	1	2	4
$\log(\gamma_{max})$	5	6	8
z (fixed)		0.34	
δ_D	1	20	100
$\log(B/G)$	-2	-1	1
$\log(t_{var}/s)$	4	5	8

Conducting the SSC fits for each blazar in our sample, we present the physical parameters of each fit in Table 3. Additionally, the SSC fit for each blazar also allows for an independent estimation for ν_{syn} , in yellow on the right panel of Figure 3. The peak frequencies and fluxes are obtained by finding all the extrema of the **agnpy** SSC fit and then evaluating which maxima are the peaks of the synchrotron and high-energy peaks. Using these located peaks, we estimate the Compton dominance ratio using

$$CD = \frac{L_{peak}^{Com}}{L_{peak}^{syn}} = \frac{F_{peak}^{Com}}{F_{peak}^{syn}} \quad (3)$$

and the characteristic Doppler boost

$$\gamma_{boost} = \left(\frac{3\nu_{Com}}{4\nu_{syn}} \right)^{1/2} \quad (4)$$

These quantities are features of the shape of the spectral fit; though highly dependent on the physical processes of the jet, they can be estimated through simple polynomial or log-normal fitting of the spectrum. The 4LAC catalog (Ajello et al. 2022) estimates these parameters for hundreds of known BL Lacs and FSRQs using non-physical methods, but our analysis of **agnpy** fits allows for direct comparison between our sample of new blazars and established catalogs of known blazars while examining underlying physical parameters. The phenomenological parameters of the **agnpy** spectral fits, plus the bolometric flux obtained by integrating under the fits, are presented in Table 2 and are available as machine-readable databases.

4. RESULTS AND CONCLUSIONS

4.1. BLaST vs. agnpy Comparison

Because both **BLaST** and **agnpy** produce estimates for ν_{syn} , it is useful to compare the two approaches, especially as both have not yet been widely used. Figure 5

plots the ν_{syn} estimates from both methods, colored by the goodness-of-fit $\chi_r^2 = \chi^2/\text{D.o.F.}$ in the **agnpy** fitting. Only **BLaST** returns an uncertainty for ν_{syn} as it is directly fitting for ν_{syn} using machine learning, while the value for ν_{syn} extracted from **agnpy** is a phenomenological estimation from the shape of the entire fitted spectrum.

Though the distribution of ν_{syn} and the blue regression line show a positive correlation, there is some scatter and the slope of the best-fit line to the two estimates is not unity, the expected result if the two estimates produced identical values for ν_{syn} . Notably, there seem to be a small number of blazars with high ν_{syn} estimated by **BLaST** but low ν_{syn} via SSC fitting. Overall, Figure 3 shows that **agnpy** tends to prefer lower ν_{syn} values for individual blazars compared to **BLaST**.

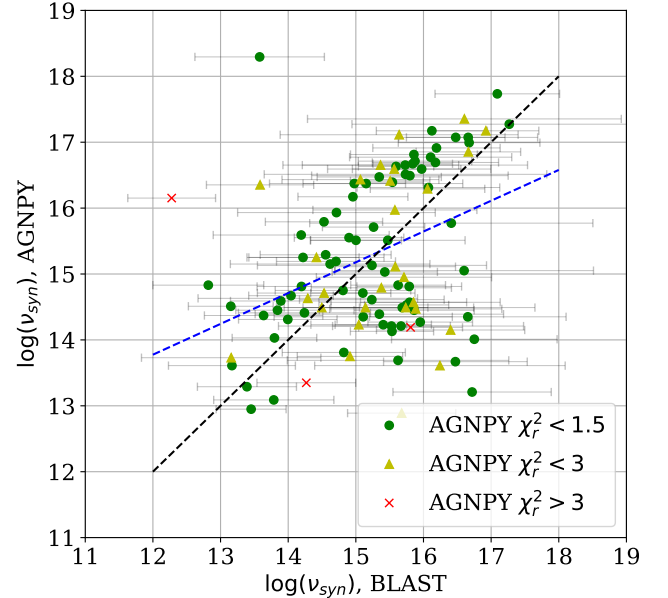


Figure 5. Comparing ν_{syn} estimates from **BLaST** and **agnpy** methods. Points are color-coded based on **agnpy** fit χ_r^2 . The dashed black line is a one-to-one correspondence, while the dashed blue line is a linear regression to the points with $\chi_r^2 < 1.5$

The most straightforward explanation for this difference is that **agnpy** fits a model including only synchrotron and synchrotron-self-Compton components, while **BLaST** was constructed to account for IR or optical contributions from other sources like dust, the disk, or galactic stars. If a particular blazar has an IR or optical excess separate from its synchrotron emission, then our simple implementation of **agnpy** would not account for that discrepancy, while **BLaST** would. This would lead to higher ν_{syn} estimates from **BLaST** via discounting IR or optical contributions from non-synchrotron processes.

Overall, both **BLaST** and **agnpy** SSC fitting are capable tools for obtaining estimates for ν_{syn} . While **agnpy** requires significantly more computation time for multi-dimensional fits to SEDs, its results can also serve to estimate phenomenological parameters like ν_{Com} and Compton dominance while constraining physical parameters. However, **BLaST** is trained to avoid deception by IR or optical excesses from non-synchrotron components. The two methods are complementary, especially for investigations focused on obtaining ν_{syn} values.

4.2. Comparisons with Bright Blazars

Both **agnpy** and **BLaST** estimations for ν_{syn} show that the new blazars tend to have higher synchrotron peaks characteristic of ISP or HSP BL Lac objects. The histograms in Figure 3 show that the **BLaST** (in green) and **agnpy** (yellow) distributions for ν_{syn} trend higher than the overall BL Lac sample from the 4LAC catalog, and have far greater ν_{syn} than the FSRQs from 4LAC. While the physical fitting of blazar SEDs via **agnpy** produced lower ν_{syn} estimates than **BLaST**, this may be due to the implicit spectral shape invoked in SSC fitting or the lack of accommodation for non-synchrotron contributions to the low-energy peak.

The blazar sequence described in [Fossati et al. \(1998\)](#) and [Ghisellini et al. \(2017\)](#) predicts an anticorrelation between gamma-ray luminosity and ν_{syn} , and our **BLaST** and **agnpy** results support this prediction for a population of dim blazars that have until now been entirely excluded from the construction of the blazar sequence.

The Compton dominance of a blazar is another key parameter of the blazar sequence, evolving alongside luminosity and ν_{syn} in that framework. [Finke \(2013\)](#) showed that absent absolute luminosity data, a version of the blazar sequence can be constructed by comparing Compton dominance ratio and synchrotron peak frequency, an approach well-suited for our sample of new, dimmer blazars lacking photometric or spectroscopic redshifts. After using the **agnpy** fits to estimate the Compton dominance ratio for the new blazars, we compare with the known BL Lacs and FSRQs of the 4LAC catalog, as well as with a more restricted HSP ($\nu_{syn} > 10^{15}$ Hz) BL Lac subsample. Figure 6 compares the distributions of these blazar samples.

The histograms in Figure 6 show that the Compton dominance ratios of the new blazars are slightly higher than for the *Fermi* BL Lacs in general and the HSP BL Lacs specifically. Conducting a two-sample T-test for equal means, we find the p-value by comparing the Compton dominance ratios of the 4LAC BL Lacs and our sample of new blazars. Obtaining a p-value of 0.007, we find evidence against the null hypothesis that the

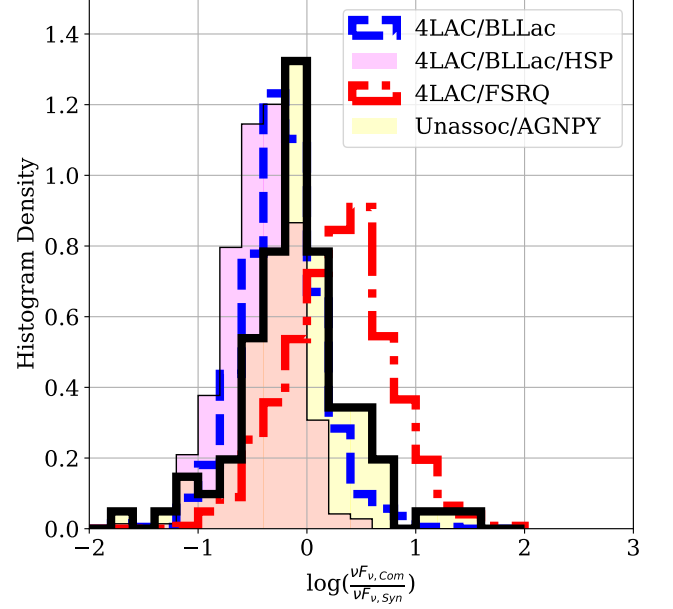


Figure 6. Compton dominance ratio for the new blazars (green) and the 4LAC FSRQs (red) and BL Lacs (blue), plus for 4LAC HSP BL Lacs (faint pink)

samples of blazar Compton dominance are drawn from the same population at the 99% threshold. The slightly higher Compton dominance distribution of our sample of new blazars represents an inversion of the expected trend of brighter FSRQs and BL Lacs.

[Finke \(2013\)](#) showed that the blazar sequence can be reframed in terms of an anticorrelation between ν_{syn} and Compton dominance, suggesting that our new blazars seem to be a break from this trend, as their Compton dominance distribution is *higher* with their greater ν_{syn} . However, one intriguing prediction of [Finke \(2013\)](#) may shed light on this tension. After physically modelling the SSC emission for blazars and predicting changes in Compton dominance along the blazar sequence, Figure 7 of [Finke \(2013\)](#) shows that for particularly high ν_{syn} blazars the theoretical Compton dominance ratio should increase as B and the energy density are increased. Because the new blazars studied in this work have notably higher ν_{syn} , the unexpected result in Figure 6 may be an indication of the inverted trend noted in [Finke \(2013\)](#).

Figure 7 reproduces Figure 5 from [Finke \(2013\)](#), with the new blazars superimposed on the 4LAC FSRQs and BL Lacs. While the new blazars tend to fall within the expected phase space in terms of Compton dominance ratio and synchrotron peak frequency estimated by **agnpy**, this comparison demonstrates that the new blazars are similar to ISP and HSP BL Lac objects, occupying the same phase-space of this version of the blazar sequence while having slightly higher Comp-

ton dominance ratios (especially at higher ν_{syn}). Further broadband observations of the new blazars could constrain the Compton dominance ratio while testing whether SSC emission models are appropriate for this sample. Even without precisely constrained redshifts, this result shows that our sample of new blazars extends the blazar sequence in terms of Compton dominance and ν_{syn} .

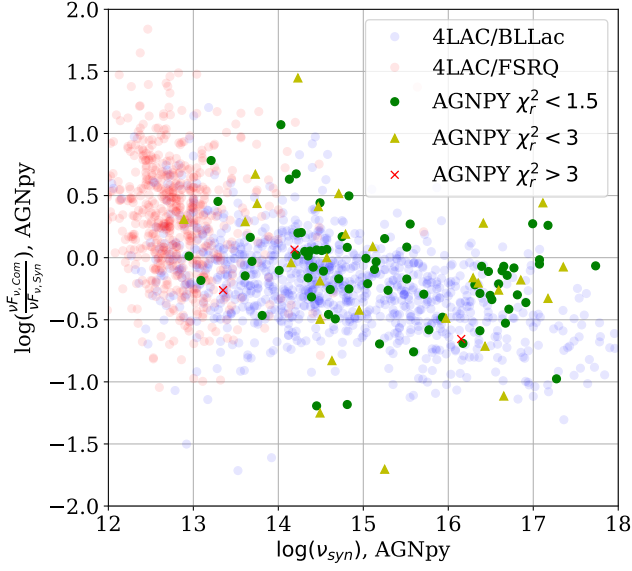


Figure 7. Compton dominance ratio for the new blazars color-coded by SSC fit reduced χ^2 , and the 4LAC FSRQs (faint red) and BL Lacs (faint blue). This figure reproduces Figure 5 in [Finke \(2013\)](#), showing that the new blazars fall within the expected range for BL Lac objects while having lightly higher Compton dominance ratios at high ν_{syn} .

The characteristic Doppler boost $\gamma_{bo} = \left(\frac{3\nu_{Com}}{4\nu_{syn}} \right)^{1/2}$ between the synchrotron and high-energy peak in a blazar’s two-hump spectrum traces a characteristic energy of the emitting electron distribution. While this parameter is a fitted physical parameter of the electron distribution, we measure it directly from the peak frequencies of each blazar spectrum. Figure 8 compares the distributions of γ_{bo} calculated from the peak positions obtained with **agnpy** to values for the known blazars of the 4LAC catalog. In agreement with the predictions of the blazar sequence framework, this phenomenological approach to measuring γ factors in an SSC emission model shows that the new blazars have sequentially lower γ_{bo} compared to the HSP BL Lacs, the BL Lacs in general, and the 4LAC FSRQs.

In spectral terms, this means that the synchrotron and high energy peak frequencies of the new blazars tend to be closer than in brighter blazars. This trend suggests

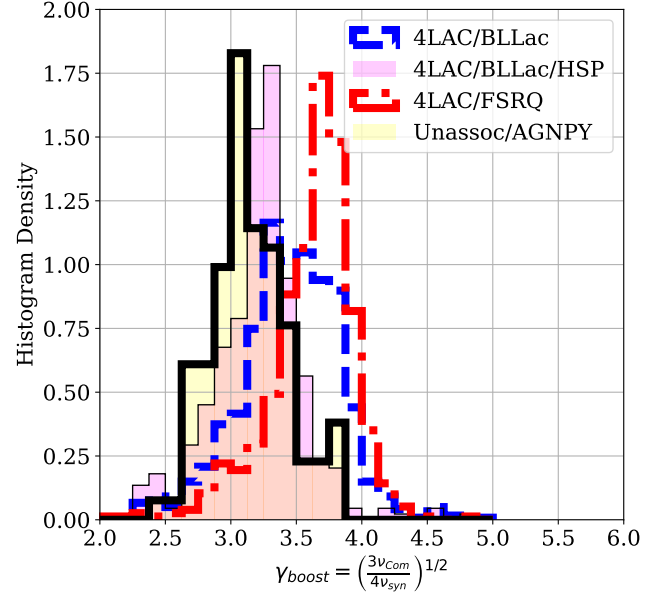


Figure 8. Characteristic Doppler boost γ_{bo} for the new blazars (green) and the 4LAC FSRQs (red) and BL Lacs (blue), plus for 4LAC HSP BL Lacs (faint pink). In agreement with the predictions of the blazar sequence, the dim blazars of the unassociated sources have sequentially lower γ_{bo} than the HSP BL Lacs of the 4LAC catalog.

that there may be astrophysical differences in the emission regions of our sample of new blazars compared to the brighter 4LAC blazars, and that our examination of the unassociated sources is revealing blazars that extend known blazar samples not only to lower flux but also to new extrema of astrophysical properties.

Using the SSC fits in [Ghisellini et al. \(2010\)](#) for a collection of bright blazars, we can compare physical jet parameters like B and electron distribution parameters with a sample of brighter blazars. Though the sample in [Ghisellini et al. \(2010\)](#) is small, it contains some of the best-studied bright blazars in the sky modeled with SSC fits similar to our **agnpy** approach, facilitating direct comparison. In Figure 9 we compare fitted parameters of the emitting electron distribution for the new blazars (green) and the BL Lac and FSRQ samples (blue dotted and red dashed). γ_b is related to the distance between the two peak frequencies of the two-hump blazar distribution, but here we show the **agnpy** fitted values for completeness.

In terms of γ_b and the two slopes of the electron distribution p_1 and p_2 , the new blazars are reasonably similar to the brighter BL Lac sample from [Ghisellini et al. \(2010\)](#). The magnetic field strength B shows more of a divergence, with the new blazars having generally lower field strength than either the known BL Lacs or FSRQs. This is similarly in agreement with the predictions of the

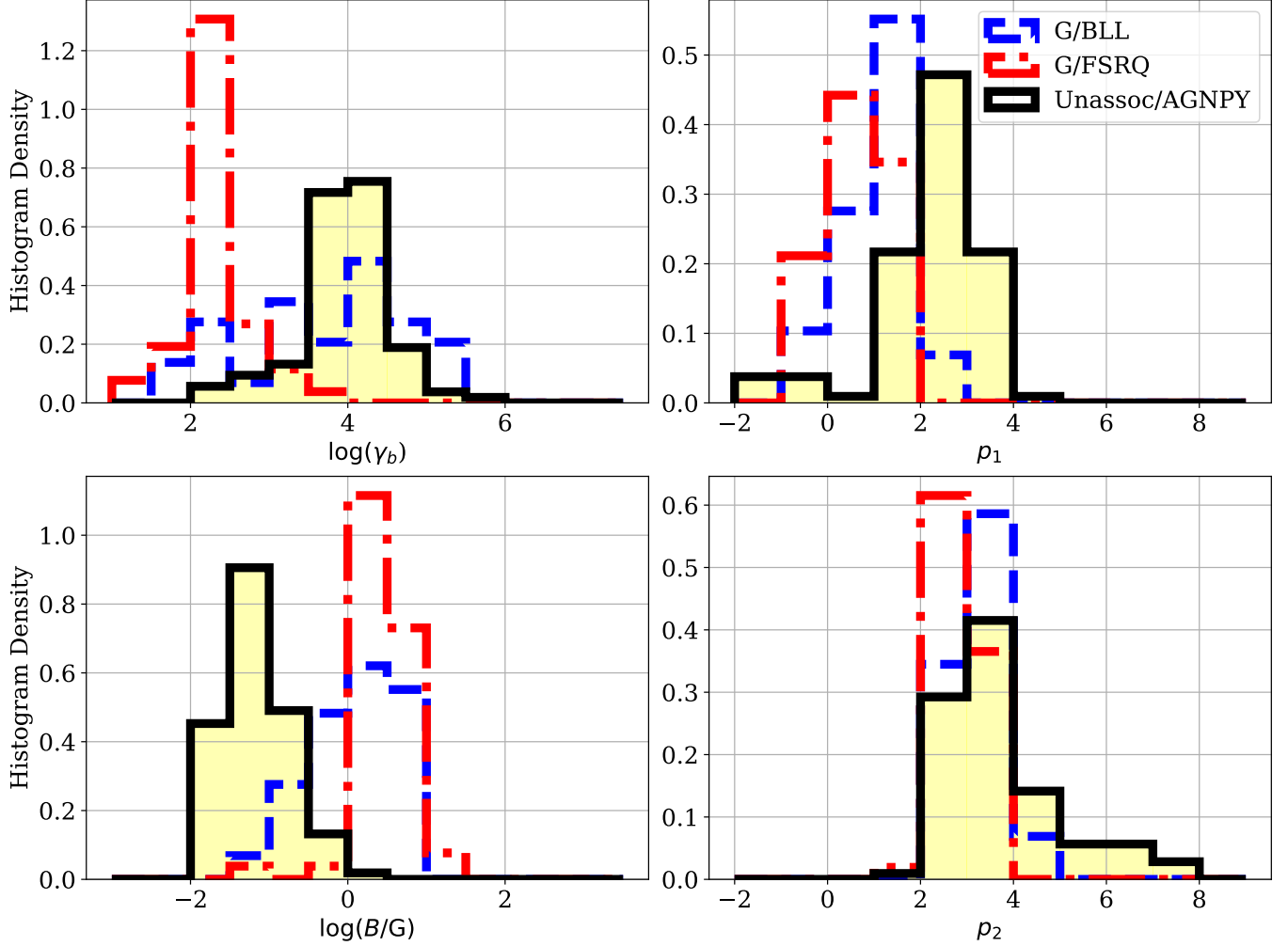


Figure 9. Physical parameters of the emitting electron distribution for the new blazars via agnpy (yellow) and a sample of BL Lacs and FSRQs (blue and red) from Ghisellini et al. (2010). Clockwise from top left, the logarithm of γ_b the break energy in the broken power law electron distribution, p_1 and p_2 the slopes before and after the break energy, and the logarithm of ambient magnetic field in Gauss.

blazar sequence described in Ghisellini et al. (2017), and together with a lower Doppler factor δ_D can explain the dimness of the new blazars. Together with the difference in peak frequency separation in Figure 8, these two plots hint at astrophysical differences in the new blazars beyond continuations of the blazar sequence.

4.3. Summary and Next Steps

Building SEDs for a sample of 106 blazars identified among the *Fermi* unassociated sources in K21, we used the recently released BLaST tool to predict ν_{syn} for each blazar. Compared to the brighter blazars of the 4LAC catalog, the new blazars have higher synchrotron peaks shown in Figure 3, characteristic of HSP BL Lacs. This finding is in agreement with the prediction of the blazar sequence framework (Ghisellini et al. 2017) that dim gamma-ray blazars will have high synchrotron peaks.

It bears noting that the alternative interpretation of the blazar sequence described in Giommi et al. (2012) argues that dim, red blazars are excluded from gamma-ray samples due to selection effects. While the new blazars investigated in this work do tend to have high synchrotron peaks in line with predictions of the blazar sequence, red dim blazars might have low enough gamma-ray fluxes to be undetected (not just unassociated) in the *Fermi* point source catalog. While our findings suggest that the blazars of the unassociated sources tend to have high ν_{syn} , we cannot rule out samples of even dimmer, redder blazars that would be entirely absent from the *Fermi* point source catalog. Still, our results extend the general findings of Ghisellini et al. (2017) to even dimmer *Fermi* blazars, showing that the blazar sequence prediction of anticorrelation between luminosity

and ν_{syn} holds for a sample of blazars previously excluded from the construction of that theory.

With **agnpy** conducting SSC fits of the blazar SEDs with fixed redshift $z = 0.34$ (the median BL Lac redshift in the 4LAC catalog), we obtained estimates for Compton dominance ratio and characteristic relativistic boost γ_{bo} . Comparing these phenomenological parameters with brighter blazars, we found that the new blazars continue the trends in magnetic field strength B and characteristic Doppler boost γ_{bo} predicted in the blazar sequence. However, we also find that the new blazars have unexpectedly high Compton dominance ratios, a result that may be related to the inverted Compton dominance trend predicted in Figure 8 of Finke (2013) for BL Lacs with particularly high ν_{syn} .

Fitting the blazar SEDs with **agnpy** also produces estimates for the physical parameters of the emitting jet and host galaxy for each blazar. While degeneracies between physical parameters make tight constraints on the emitting region difficult, comparing jet parameter estimates to SSC fits of brighter blazars Ghisellini et al. (2010) show that the new blazars have broadly similar physical parameters to brighter blazars, shown in Figure 9. The magnetic field strength B does seem to be slightly lower for the new blazars than for the brighter blazars, another hint at physical differences between the 4LAC blazars and these new blazars from the unassociated sample. Alternatively, the SSC emission model used for **agnpy** fitting may not be the best phenomenological model for these dim blazars; while many bright blazars are adequately described by SSC, further observations at these dim blazars may characterize their spectra enough to allow for comparisons with proton cascade (Mannheim 1993), external Compton (Sikora et al. 1994), or proton synchrotron (Mücke & Protheroe 2001; Mücke et al. 2003) models. An alternative emission mechanism may also explain the noticeably higher Compton dominance ratio shown in Figure 6.

Further targeted observations could constrain physical parameters of individual blazars and firmly estab-

lish their relationship with the wider blazar population. Establishing photometric or spectroscopic redshifts of a subset of our low-luminosity blazar sample would firmly constrain the absolute gamma-ray luminosity of each object and more confidently place each in the context of the blazar sequence. Given that our results suggest that many of these blazars are BL Lac objects, it may be difficult to obtain spectroscopic redshifts of such dim sources lacking optical lines.

We chose an SSC model to fit the blazar SEDs for its simplicity and its phenomenological flexibility, but for many brighter blazars more complex models are necessary. Investigating new blazars in our sample that are not well fit by the SSC model can be used to double-check our sample for incorrect inclusions while allowing for exploring alternative emission mechanisms. Just as K21 investigated unusual or unique unassociated sources from the wider catalog, the SEDs constructed in Section 2.2 are a starting point for individual analysis. Similarly, creating SEDs of unassociated targets that fit neither blazar nor pulsar classification in K21 would clarify the nature of the remaining unclassified sources.

Software: Astropy (The Astropy Collaboration et al. 2013), numpy (Harris et al. 2020), Matplotlib (Hunter 2007), FTools (Blackburn 1995), agnpy (Nigro et al. 2022), BLaST (Glauch et al. 2022)

ACKNOWLEDGMENTS

This research has made use of data and/or software provided by the High Energy Astrophysics Science Archive Research Center (HEASARC), which is a service of the Astrophysics Science Division at NASA/GSFC. We gratefully acknowledge the support of NASA grants 80NSSC17K0752 and 80NSSC18K1730. Finally, we are grateful for the helpful comments and suggestions of our anonymous reviewer.

REFERENCES

- Abdo, A. A., Ackermann, M., Ajello, M., et al. 2010a, ApJ, 722, 520, doi: [10.1088/0004-637X/722/1/520](https://doi.org/10.1088/0004-637X/722/1/520)
- Abdo, A. A., Ackermann, M., Agudo, I., et al. 2010b, ApJ, 716, 30, doi: [10.1088/0004-637X/716/1/30](https://doi.org/10.1088/0004-637X/716/1/30)
- Abdollahi, S., Acero, F., Ackermann, M., et al. 2020, ApJS, 247, 33, doi: [10.3847/1538-4365/ab6bcb](https://doi.org/10.3847/1538-4365/ab6bcb)
- Abdollahi, S., Acero, F., Baldini, L., et al. 2022, ApJS, 260, 53, doi: [10.3847/1538-4365/ac6751](https://doi.org/10.3847/1538-4365/ac6751)
- Ajello, M., Angioni, R., Axelsson, M., et al. 2020, ApJ, 892, 105, doi: [10.3847/1538-4357/ab791e](https://doi.org/10.3847/1538-4357/ab791e)
- Ajello, M., Baldini, L., Ballet, J., et al. 2022, arXiv e-prints, arXiv:2209.12070. <https://arxiv.org/abs/2209.12070>
- Bianchin, V., Foschini, L., Ghisellini, G., et al. 2009, A&A, 496, 423, doi: [10.1051/0004-6361/200811128](https://doi.org/10.1051/0004-6361/200811128)

- Blackburn, J. K. 1995, in *Astronomical Society of the Pacific Conference Series*, Vol. 77, *Astronomical Data Analysis Software and Systems IV*, ed. R. A. Shaw, H. E. Payne, & J. J. E. Hayes, 367
- Blandford, R. D., & Rees, M. J. 1978, *Physica Scripta*, 17, 265, doi: [10.1088/0031-8949/17/3/020](https://doi.org/10.1088/0031-8949/17/3/020)
- Celotti, A., & Ghisellini, G. 2008, *MNRAS*, 385, 283, doi: [10.1111/j.1365-2966.2007.12758.x](https://doi.org/10.1111/j.1365-2966.2007.12758.x)
- Condon, J. J., Cotton, W. D., Greisen, E. W., et al. 1998, *AJ*, 115, 1693, doi: [10.1086/300337](https://doi.org/10.1086/300337)
- Cutri, R. M., & et al. 2012, *VizieR Online Data Catalog*, II/311
- Dermer, C. D., & Schlickeiser, R. 1993, *ApJ*, 416, 458, doi: [10.1086/173251](https://doi.org/10.1086/173251)
- Finke, J. D. 2013, *ApJ*, 763, 134, doi: [10.1088/0004-637X/763/2/134](https://doi.org/10.1088/0004-637X/763/2/134)
- Finke, J. D., Dermer, C. D., & Böttcher, M. 2008, *ApJ*, 686, 181, doi: [10.1086/590900](https://doi.org/10.1086/590900)
- Fossati, G., Maraschi, L., Celotti, A., Comastri, A., & Ghisellini, G. 1998, *Monthly Notices of the Royal Astronomical Society*, 299, 433, doi: [10.1046/j.1365-8711.1998.01828.x](https://doi.org/10.1046/j.1365-8711.1998.01828.x)
- Ghisellini, G., Righi, C., Costamante, L., & Tavecchio, F. 2017, *Monthly Notices of the Royal Astronomical Society*, Volume 469, Issue 1, p.255-266, 469, 255, doi: [10.1093/mnras/stx806](https://doi.org/10.1093/mnras/stx806)
- Ghisellini, G., & Tavecchio, F. 2008, *Monthly Notices of the Royal Astronomical Society*, doi: [10.1111/j.1365-2966.2008.13360.x](https://doi.org/10.1111/j.1365-2966.2008.13360.x)
- Ghisellini, G., Tavecchio, F., Foschini, L., et al. 2010, *MNRAS*, 402, 497, doi: [10.1111/j.1365-2966.2009.15898.x](https://doi.org/10.1111/j.1365-2966.2009.15898.x)
- Giommi, P., & Padovani, P. 2015, *MNRAS*, 450, 2404, doi: [10.1093/mnras/stv793](https://doi.org/10.1093/mnras/stv793)
- Giommi, P., Padovani, P., Polenta, G., et al. 2012, *MNRAS*, 420, 2899, doi: [10.1111/j.1365-2966.2011.20044.x](https://doi.org/10.1111/j.1365-2966.2011.20044.x)
- Glauch, T., Kerscher, T., & Giommi, P. 2022, *Astronomy and Computing*, 41, 100646, doi: [10.1016/j.ascom.2022.100646](https://doi.org/10.1016/j.ascom.2022.100646)
- Gordon, Y. A., Boyce, M. M., O’Dea, C. P., et al. 2021, *VizieR Online Data Catalog*, J/ApJS/255/30
- Harris, C. R., Millman, K. J., van der Walt, S. J., et al. 2020, *Nature*, 585, 357, doi: [10.1038/s41586-020-2649-2](https://doi.org/10.1038/s41586-020-2649-2)
- Hunter, J. D. 2007, *Computing in Science and Engineering*, 9, 90, doi: [10.1109/MCSE.2007.55](https://doi.org/10.1109/MCSE.2007.55)
- Kaur, A., Kerby, S., & Falcone, A. D. 2023, *ApJ*, 943, 167, doi: [10.3847/1538-4357/ac8b80](https://doi.org/10.3847/1538-4357/ac8b80)
- Kerby, S., Kaur, A., Falcone, A. D., et al. 2021, *ApJ*, 923, 75, doi: [10.3847/1538-4357/ac2e91](https://doi.org/10.3847/1538-4357/ac2e91)
- Lott, B., Gasparrini, D., & Ciprini, S. 2020, *arXiv e-prints*, arXiv:2010.08406. <https://arxiv.org/abs/2010.08406>
- Mannheim, K. 1993, *A&A*, 269, 67. <https://arxiv.org/abs/astro-ph/9302006>
- Maraschi, L., Ghisellini, G., & Celotti, A. 1992, *ApJL*, 397, L5, doi: [10.1086/186531](https://doi.org/10.1086/186531)
- Mauch, T., Murphy, T., Buttery, H. J., et al. 2003, *MNRAS*, 342, 1117, doi: [10.1046/j.1365-8711.2003.06605.x](https://doi.org/10.1046/j.1365-8711.2003.06605.x)
- Mücke, A., & Protheroe, R. J. 2001, *Astroparticle Physics*, 15, 121, doi: [10.1016/S0927-6505\(00\)00141-9](https://doi.org/10.1016/S0927-6505(00)00141-9)
- Mücke, A., Protheroe, R. J., Engel, R., Rachen, J. P., & Stanev, T. 2003, *Astroparticle Physics*, 18, 593, doi: [10.1016/S0927-6505\(02\)00185-8](https://doi.org/10.1016/S0927-6505(02)00185-8)
- Nelder, J. A., & Mead, R. 1965, *The Computer Journal*, 7, 308, doi: [10.1093/comjnl/7.4.308](https://doi.org/10.1093/comjnl/7.4.308)
- Nigro, C., Sitarek, J., Gliwny, P., et al. 2022, *A&A*, 660, A18, doi: [10.1051/0004-6361/202142000](https://doi.org/10.1051/0004-6361/202142000)
- Sikora, M., Begelman, M. C., & Rees, M. J. 1994, *ApJ*, 421, 153, doi: [10.1086/173633](https://doi.org/10.1086/173633)
- Stickel, M., Padovani, P., Urry, C. M., Fried, J. W., & Kuehr, H. 1991, *ApJ*, 374, 431, doi: [10.1086/170133](https://doi.org/10.1086/170133)
- Tavecchio, F., Maraschi, L., & Ghisellini, G. 1998, *ApJ*, 509, 608, doi: [10.1086/306526](https://doi.org/10.1086/306526)
- The Astropy Collaboration, Robitaille, Thomas P., Tollerud, Erik J., et al. 2013, *A&A*, 558, A33, doi: [10.1051/0004-6361/201322068](https://doi.org/10.1051/0004-6361/201322068)
- Urry, C. M., & Padovani, P. 1995, *PASP*, 107, 803, doi: [10.1086/133630](https://doi.org/10.1086/133630)
- Wilms, J., Allen, A., & McCray, R. 2000, *ApJ*, 542, 914, doi: [10.1086/317016](https://doi.org/10.1086/317016)

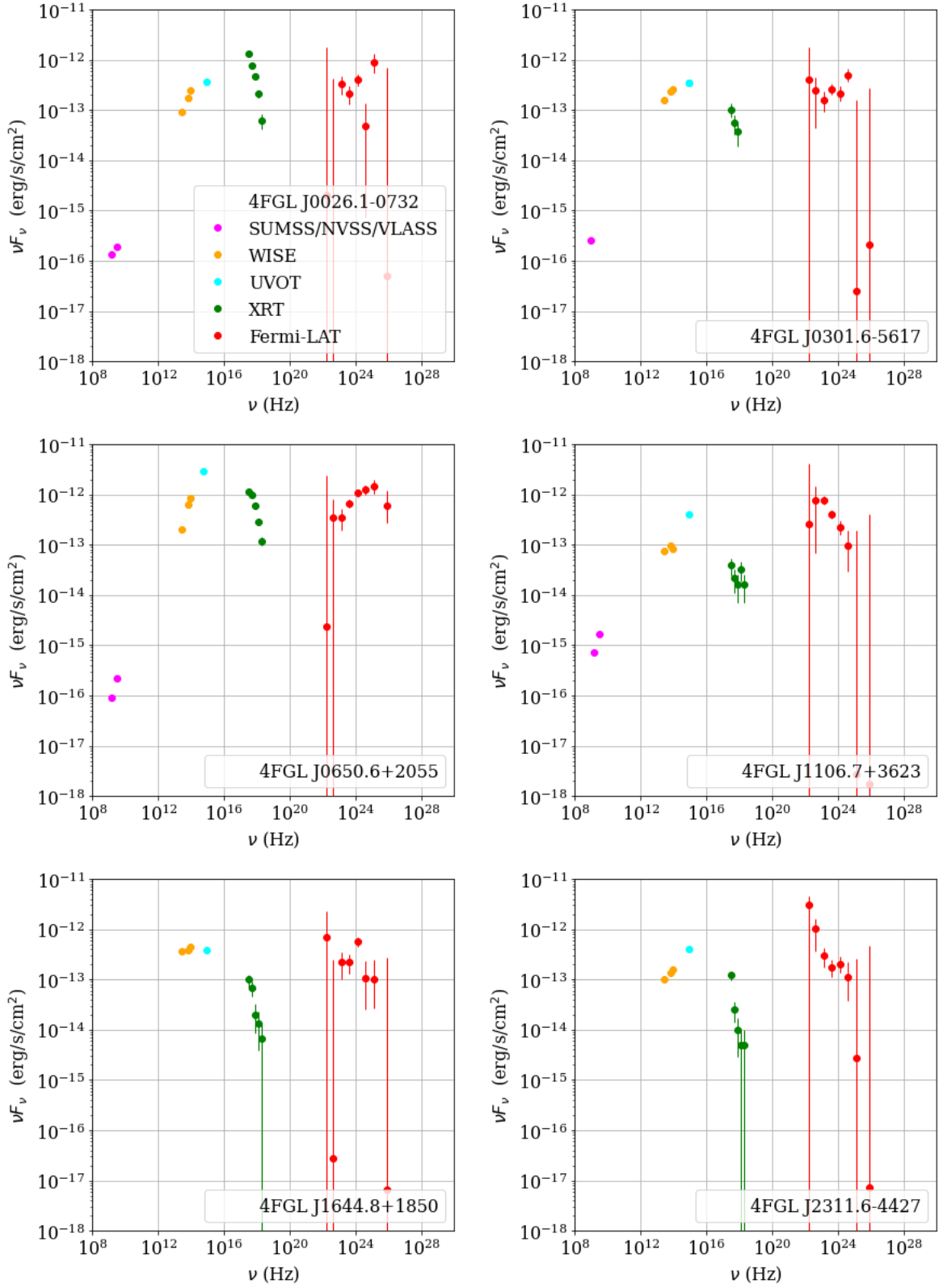


Figure 10. Representative SEDs for a small selection of the 106 blazars examined in this work.

Table 2. Phenomological features of the broadband SEDs from agnpy fitting unless otherwise noted

4FGL	XRT	$\log(\nu_{syn, BLAST})$	$\log(\delta\nu_{syn, BLAST})$	$\log(\nu_{syn})$	$\log(\nu F_{\nu, syn})$	$\log(\nu Com)$	$\log(\nu F_{\nu, Com})$	$\log(F_{bol})$
		$\log(\text{Hz})$	$\log(\text{Hz})$	$\log(\text{Hz})$	$\log(\text{erg/s/cm}^2)$	$\log(\text{Hz})$	$\log(\text{erg/s/cm}^2)$	$\log(\text{erg/s/cm}^2)$
J0004.4-4001	J000434.1-400036	14.707	0.626	15.191	-11.728	23.7	-12.423	-9.545
J0025.4-4838	J002536.8-483808	15.794	1.326	14.571	-12.304	22.519	-12.238	-9.931
J0026.1-0732	J002611.9-073115	16.6	0.829	15.051	-12.444	23.84	-12.654	-10.01
J0031.5-5648	J003135.1-564640	15.595	1.047	16.633	-12.51	24.601	-12.615	-10.058
J0037.2-2653	J003729.6-265043	13.787	1.759	13.089	-12.449	21.297	-12.633	-9.975
J0057.9+6326	J005758.1+632642	15.678	0.708	12.889	-12.545	21.197	-12.237	-9.693
J0058.3-4603	J005806.4-460417	17.091	0.821	17.734	-12.773	24.801	-12.839	-10.215
J0118.3-6008	J011823.10-600753	14.24	1.155	14.411	-12.248	23.119	-12.325	-9.916
J0120.2-7944	J011914.7-794509	15.861	1.318	14.451	-12.586	22.679	-12.524	-10.171
J0125.9-6303	J012548.3-630244	16.073	0.771	16.312	-12.599	24.401	-12.817	-10.123
J0156.3-2420	J015624.4-242004	15.712	0.712	14.951	-11.923	24.521	-12.346	-9.708
J0159.0+3313	J015905.0+331254	15.737	0.838	14.491	-12.324	24.04	-12.511	-9.903
J0209.8+2626	J020946.5+262528	16.719	1.143	13.209	-12.906	21.518	-12.123	-9.795
J0231.0+3505	J023112.4+350446	16.664	0.933	16.853	-12.721	24.381	-12.901	-10.171
J0240.2-0248	J024004.6-024504	14.822	0.649	13.81	-11.782	21.938	-12.247	-9.597
J0259.0+0552	J025857.4+055243	15.377	0.625	14.791	-12.062	24.04	-11.873	-9.598
J0301.6-5617	J030115.2-561647	14.554	1.913	15.291	-12.401	23.94	-12.664	-9.962
J0302.5+3354	J030226.7+335447	15.73	0.813	16.653	-12.605	23.78	-12.675	-9.99
J0327.6+2620	J032737.2+262007	15.973	0.772	16.593	-12.521	24.741	-12.732	-10.018
J0406.2+0639	J040607.7+063918	15.405	1.295	14.23	-12.773	22.959	-12.575	-10.107
J0409.2+2542	J040921.6+254440	15.734	0.889	16.513	-12.129	25.101	-12.467	-9.803
J0427.8-6704	J042749.5-670435	15.044	2.093	14.23	-13.143	22.338	-11.696	-9.422
J0537.5+0959	J053745.9+095759	15.583	0.957	15.111	-12.786	23.96	-12.697	-10.096
J0539.2-6333	J054002.9-633216	14.192	1.023	15.592	-11.928	24.361	-12.686	-9.758
J0610.8-4911	J061031.8-491222	14.529	0.557	15.792	-9.862	23.98	-12.752	-8.073
J0610.8-4911	J061100.0-491034	16.655	1.273	14.35	-12.874	23.84	-12.861	-10.134
J0620.7-5034	J062045.7-503349	15.348	0.615	14.391	-12.439	23.56	-12.756	-9.939
J0633.9+5840	J063400.1+584035	14.913	1.062	13.75	-13.233	23.72	-12.796	-10.34

Table 2 continued

Table 2 (continued)

4FGL	XRT	$\log(\nu_{syn, BLAST})$	$\log(\delta\nu_{syn, BLAST})$	$\log(\nu_{syn})$	$\log(\nu F_{\nu, syn})$	$\log(\nu Com)$	$\log(\nu F_{\nu, Com})$	$\log(F_{bol})$
		$\log(\text{Hz})$	$\log(\text{Hz})$	$\log(\text{Hz})$	$\log(\text{erg/s/cm}^2)$	$\log(\text{Hz})$	$\log(\text{erg/s/cm}^2)$	$\log(\text{erg/s/cm}^2)$
J0650.6+2055	J065035.4+205556	16.411	1.055	15.772	-11.331	24.741	-11.912	-9.148
J0704.3+4829	J070421.8+482645	16.177	0.871	16.693	-12.376	24.461	-12.518	-9.914
J0738.6+1311	J073843.4+131330	14.496	0.517	14.491	-10.78	22.499	-12.031	-8.916
J0800.1+5531	J075949.3+553253	13.891	1.17	14.591	-11.896	22.739	-12.353	-9.694
J0800.1+5531	J080013.1+553407	13.636	1.808	14.371	-12.287	22.439	-12.235	-9.934
J0800.9+0733	J080056.5+073235	15.365	0.779	16.653	-12.037	24.701	-13.152	-9.849
J0838.5+4013	J083902.8+401548	15.142	0.782	14.491	-12.593	23.239	-13.089	-10.111
J0903.5+4057	J090342.8+405502	14.977	0.846	16.373	-12.683	24.0	-12.97	-10.228
J0906.1+1011	J090616.2+101430	14.9	1.836	15.552	-12.787	22.999	-12.516	-9.981
J0910.1+1816	J091003.9+181613	15.853	0.986	14.571	-12.69	23.039	-12.69	-10.113
J0914.5+6845	J091429.10+684509	15.799	0.923	16.493	-12.321	24.601	-12.624	-9.91
J0928.4+5256	J092818.7+525700	15.527	1.159	14.21	-12.696	23.099	-12.021	-9.696
J0930.9+3030	J093058.0+303118	15.79	0.774	14.811	-12.609	24.14	-12.527	-10.051
J0934.5+7223	J093334.0+722101	13.994	1.475	14.31	-12.127	22.238	-12.077	-9.744
J0938.8+5155	J093835.0+515455	13.151	1.428	14.511	-12.712	22.459	-12.655	-10.102
J1008.2+1000	J100749.3+094910	13.157	1.224	13.73	-12.439	21.518	-11.767	-9.632
J1008.2+1000	J100802.5+095918	12.278	0.672	16.152	-12.596	23.239	-13.251	-10.128
J1008.2+1000	J100848.6+095450	13.842	0.921	14.451	-10.533	22.459	-11.726	-8.724
J1011.1+4420	J101132.0+442254	17.268	0.773	17.273	-11.651	25.822	-12.627	-9.484
J1016.1+4247	J101620.8+424723	15.577	0.617	15.972	-11.587	24.701	-12.075	-9.519
J1018.1+2705	J101750.2+270550	15.534	1.811	14.13	-12.655	22.118	-12.023	-9.672
J1018.1+4051	J101801.5+405520	13.584	1.911	16.352	-12.594	23.36	-12.798	-10.061
J1018.1+4051	J101807.6+404407	13.452	2.088	12.949	-12.732	23.179	-12.719	-10.106
J1024.5+4543	J102432.6+454428	16.675	0.985	16.993	-12.767	24.12	-12.494	-9.985
J1034.7+4645	J103438.7+464404	16.472	0.91	13.67	-12.701	22.759	-12.537	-10.088
J1048.4+5030	J104824.2+502941	15.068	0.656	16.433	-11.817	25.021	-12.53	-9.679
J1049.8+2741	J104938.8+274217	15.567	0.756	16.593	-12.44	24.2	-12.701	-10.005
J1106.7+3623	J110636.7+362648	12.819	1.301	14.831	-12.732	22.979	-12.235	-9.964
J1111.4+0137	J111114.2+013430	16.401	1.622	14.15	-12.606	23.039	-12.646	-10.179
J1119.9+1007	J111948.2+100704	15.428	0.701	15.031	-12.428	23.42	-12.434	-9.85

Table 2 continued

Table 2 (continued)

4FGL	XRT	$\log(\nu_{syn, BLAST})$	$\log(\delta\nu_{syn, BLAST})$	$\log(\nu_{syn})$	$\log(\nu F_{\nu, syn})$	$\log(\nu Com)$	$\log(\nu F_{\nu, Com})$	$\log(F_{bol})$
		$\log(\text{Hz})$	$\log(\text{Hz})$	$\log(\text{Hz})$	$\log(\text{erg/s/cm}^2)$	$\log(\text{Hz})$	$\log(\text{erg/s/cm}^2)$	$\log(\text{erg/s/cm}^2)$
J1122.0-0231	J112213.8-022916	15.625	0.82	14.831	-12.156	23.259	-12.408	-9.832
J1146.0-0638	J114600.8-063850	16.06	0.875	16.292	-12.033	25.201	-12.195	-9.731
J1155.2-1111	J115514.7-111125	15.624	0.728	13.69	-12.906	23.58	-12.936	-10.284
J1220.1-2458	J122014.5-245949	16.661	0.976	17.073	-12.416	24.3	-12.433	-9.87
J1243.7+1727	J124351.6+172643	15.236	0.622	14.611	-12.544	23.66	-12.801	-10.126
J1256.8+5329	J125630.4+533203	13.797	2.319	14.03	-13.105	22.058	-12.034	-9.816
J1326.0+3507	J132544.4+350450	14.81	0.999	14.751	-12.474	23.279	-12.305	-9.902
J1326.0+3507	J132622.3+350627	14.219	2.325	15.251	-12.473	23.8	-12.319	-9.989
J1415.9-1504	J141546.1-150228	15.109	1.199	14.35	-12.315	23.099	-12.478	-9.94
J1429.8-0739	J142949.7-073302	14.268	1.069	13.349	-12.446	23.139	-12.708	-9.931
J1513.0-3118	J151244.8-311648	14.417	0.588	15.251	-10.565	23.44	-12.269	-8.635
J1514.8+4448	J151450.10+444957	14.531	1.852	14.711	-12.316	23.119	-11.8	-9.728
J1528.4+2004	J152835.10+200423	16.477	1.002	17.073	-12.868	24.461	-12.92	-10.319
J1545.0-6642	J154459.0-664147	16.923	0.941	17.173	-11.756	25.442	-12.084	-9.493
J1557.2+3822	J155711.9+382032	15.668	0.778	14.21	-13.033	23.239	-13.012	-10.488
J1631.8+4144	J163146.7+414634	15.875	0.867	16.713	-12.233	25.221	-12.648	-9.961
J1637.5+3005	J163728.2+300957	13.168	1.453	13.61	-12.884	22.839	-13.03	-10.308
J1637.5+3005	J163739.3+301015	13.39	0.968	13.289	-12.06	20.937	-11.607	-9.482
J1644.8+1850	J164457.3+185149	14.713	1.026	15.932	-12.152	23.74	-12.632	-9.843
J1645.0+1654	J164500.0+165510	15.751	0.793	14.531	-12.524	23.44	-12.632	-10.031
J1651.7-7241	J165151.5-724309	14.62	1.34	15.151	-12.814	23.079	-12.846	-10.141
J1720.6-5144	J172032.7-514413	16.751	0.938	14.01	-12.34	24.12	-12.443	-9.766
J1818.5+2533	J181830.9+253707	14.042	0.809	14.671	-11.372	22.358	-11.864	-9.327
J1846.9-0227	J184650.7-022903	14.29	0.455	14.631	-10.252	22.959	-11.081	-8.262
J1910.8+2856	J191052.2+285624	16.243	0.938	13.61	-12.646	23.9	-12.356	-9.751
J1910.8+2856	J191059.4+285635	15.686	0.888	14.491	-12.703	24.601	-12.261	-9.941
J1918.0+0331	J191803.6+033030	15.64	0.88	17.113	-12.641	25.281	-12.199	-9.867
J1927.5+0154	J192731.3+015356	15.859	0.729	16.813	-12.155	24.781	-12.454	-9.782
J1955.3-5032	J195512.5-503011	15.885	1.212	14.471	-12.678	22.178	-12.267	-9.875
J2008.4+1619	J200827.6+161843	15.952	1.637	14.27	-12.715	23.339	-12.513	-9.995

Table 2 continued

Table 2 (*continued*)

4FGL	XRT	$\log(\nu_{syn, BLAST})$	$\log(\delta\nu_{syn, BLAST})$	$\log(\nu_{syn})$	$\log(\nu F_{\nu, syn})$	$\log(\nu Com)$	$\log(\nu F_{\nu, Com})$	$\log(\dot{F}_{bol})$
		$\log(\text{Hz})$	$\log(\text{Hz})$	$\log(\text{Hz})$	$\log(\text{erg/s/cm}^2)$	$\log(\text{Hz})$	$\log(\text{erg/s/cm}^2)$	$\log(\text{erg/s/cm}^2)$
J2041.1-6138	J204111.10-613952	15.262	0.732	15.712	-12.139	24.24	-12.433	-9.698
J2046.9-5409	J204700.5-541246	15.239	1.461	15.131	-12.586	24.28	-12.681	-10.058
J2109.6+3954	J210936.4+395513	15.81	0.744	14.19	-12.945	24.32	-12.879	-10.276
J2114.9-3326	J211452.0-332532	16.192	1.054	16.913	-12.011	24.621	-12.372	-9.648
J2159.6-4620	J215935.9-461954	15.54	0.758	16.393	-12.285	24.421	-12.354	-9.819
J2207.1+2222	J220704.3+222234	15.346	0.627	16.473	-12.51	24.481	-12.621	-10.024
J2222.9+1507	J222253.9+151052	14.957	0.89	16.172	-12.133	23.38	-12.823	-9.749
J2225.8-0804	J222552.9-080415	15.472	1.036	15.512	-12.651	24.04	-12.566	-10.077
J2237.2-6726	J223709.3-672614	16.106	0.784	16.773	-12.537	24.22	-12.62	-10.019
J2240.3-5241	J224017.5-524117	15.002	0.73	15.512	-11.957	24.2	-12.129	-9.548
J2247.7-5857	J224744.10-585500	15.508	1.453	16.413	-12.92	23.139	-12.642	-10.082
J2303.9+5554	J230351.7+555618	16.605	0.8	17.353	-12.483	24.781	-12.558	-9.951
J2311.6-4427	J231145.6-443220	15.104	1.693	14.711	-12.448	23.279	-12.618	-10.161
J2317.7+2839	J231740.0+283954	15.152	0.556	16.373	-11.613	25.502	-12.201	-9.519
J2326.9-4130	J232653.2-412713	13.578	1.096	18.294	-13.669	22.819	-12.335	-9.453
J2336.9-8427	J233627.1-842648	16.124	0.918	17.173	-12.867	23.84	-12.607	-10.061
J2337.7-2903	J233730.2-290240	15.841	0.768	16.673	-12.22	23.98	-12.747	-9.871
J2351.4-2818	J235136.5-282154	14.196	0.587	14.811	-11.302	22.899	-12.485	-9.208

Table 3. Synchrotron-self-Compton fits via agnpy with fixed $z = 0.34$

4FGL	XRT	$\log(k_e)$	p_1	p_2	$\log(\gamma_b)$	$\log(\gamma_{max})$	$\log(\gamma_{min})$	δ_D	$\log(B)$	$\log(t_{var})$	χ_r^2
									G	s	
J0004.4-4001	J000434.1-400036	-6.652	2.19	4.6	4.402	5.485	2.17	16.323	-1.151	5.309	0.715
J0025.4-4838	J002536.8-483808	-5.0	4.0	3.731	4.298	7.677	3.493	10.579	-0.382	4.377	0.805
J0026.1-0732	J002611.9-073115	-4.848	2.06	3.453	4.094	6.061	1.945	10.928	-0.803	4.925	1.469
J0031.5-5648	J003135.1-564640	-1.621	-1.002	2.738	2.983	5.407	3.38	24.931	-1.241	4.196	0.581
J0037.2-2653	J003729.6-265043	-1.965	-0.931	3.383	3.165	5.661	2.903	23.844	-1.496	4.57	0.648
J0057.9+6326	J005758.1+632642	-0.371	-1.195	3.317	2.847	7.059	2.861	11.405	-0.976	4.728	2.952
J0058.3-4603	J005806.4-460417	-5.625	3.451	2.45	4.433	5.742	3.368	8.202	-0.521	4.646	0.499
J0118.3-6008	J011823.10-600753	-4.495	3.372	3.704	4.001	5.652	3.743	13.172	-1.21	5.042	1.048
J0120.2-7944	J011914.7-794509	-4.808	3.996	3.482	4.254	5.741	3.613	12.8	-0.743	4.352	0.994
J0125.9-6303	J012548.3-630244	-4.863	3.999	2.953	3.94	5.663	3.693	17.898	-1.352	4.851	0.791
J0156.3-2420	J015624.4-242004	-4.826	-1.287	3.453	3.997	5.66	3.983	22.157	-1.395	4.889	1.503
J0159.0+3313	J015905.0+331254	-4.958	2.907	3.237	4.046	5.623	3.61	13.411	-1.082	5.006	2.018
J0209.8+2626	J020946.5+262528	-2.653	1.552	3.419	3.633	5.017	2.626	14.686	-1.955	4.971	1.001
J0231.0+3505	J023112.4+350446	-3.452	1.707	2.968	3.443	5.997	3.54	12.505	-1.248	5.127	1.857
J0240.2-0248	J024004.6-024504	-6.936	3.707	3.875	4.443	6.084	3.463	21.781	-1.422	5.024	1.218
J0259.0+0552	J025857.4+055243	-3.798	2.439	3.645	3.927	5.822	3.975	13.722	-1.303	5.027	1.848
J0301.6-5617	J030115.2-561647	-6.674	2.476	4.047	4.607	6.218	2.136	20.002	-1.524	4.911	0.93
J0302.5+3354	J030226.7+335447	-4.213	2.438	2.869	3.72	5.665	2.331	15.674	-1.382	4.962	1.119
J0327.6+2620	J032737.2+262007	-6.034	2.23	2.896	4.235	5.863	2.406	16.458	-1.688	5.264	0.81
J0406.2+0639	J040607.7+063918	-3.654	1.7	3.318	3.757	5.662	1.034	6.628	-0.864	5.297	1.219
J0409.2+2542	J040921.6+254440	-8.412	2.401	6.258	5.307	6.283	2.352	22.337	-1.56	4.815	0.762
J0427.8-6704	J042749.5-670435	-3.284	2.509	4.659	4.34	7.908	3.008	22.282	-1.979	4.0	1.647
J0537.5+0959	J053745.9+095759	-5.297	2.529	3.117	4.246	5.645	2.365	12.992	-1.252	4.911	2.84
J0539.2-6333	J054002.9-633216	-7.435	2.357	5.257	4.687	7.341	3.11	18.911	-1.245	5.131	0.987
J0610.8-4911	J061031.8-491222	-7.499	-0.87	7.997	3.996	5.399	3.634	31.275	-0.189	5.427	1.391
J0610.8-4911	J061100.0-491034	-5.528	3.11	3.057	4.486	7.949	3.296	11.25	-0.501	4.326	0.526
J0620.7-5034	J062045.7-503349	-6.098	2.392	3.208	4.168	5.824	2.366	23.116	-1.997	5.29	1.155
J0633.9+5840	J063400.1+584035	-4.26	1.634	3.176	3.874	6.027	2.417	9.387	-1.842	5.518	1.668

Table 3 *continued*

Table 3 (continued)

4FGL	XRT	$\log(k_e)$	p_1	p_2	$\log(\gamma_b)$	$\log(\gamma_{max})$	$\log(\gamma_{min})$	δ_D	$\log(B)$	$\log(t_{var})$	χ_r^2
									G	S	
J0650.6+2055	J065035.4+205556	-6.215	1.406	3.426	4.368	5.501	1.191	18.074	-0.957	5.074	0.345
J0704.3-4829	J070421.8-482645	-4.976	2.966	2.866	4.088	5.503	3.554	13.8	-0.949	4.788	0.371
J0738.6+1311	J073843.4+131330	-5.288	3.626	4.994	3.796	6.016	3.619	27.845	-1.064	5.195	2.574
J0800.1-5531	J075949.3-553253	-5.13	1.823	4.307	4.008	7.438	2.406	10.272	-0.88	5.433	0.546
J0800.1-5531	J080013.1-553407	-3.446	3.999	3.994	3.85	6.603	3.546	11.35	-0.7	4.616	0.98
J0800.9+0733	J080056.5+073235	-3.343	1.596	2.511	2.749	5.461	2.478	14.0	-1.23	5.537	2.624
J0838.5+4013	J083902.8+401548	-5.27	2.525	3.14	3.932	5.583	2.238	17.695	-1.348	5.032	1.662
J0903.5+4057	J090342.8+405502	-4.187	2.162	2.792	3.631	5.461	2.416	12.706	-1.217	5.091	0.633
J0906.1-1011	J090616.2-101430	-6.327	2.942	3.476	4.74	5.42	2.808	13.53	-0.858	4.454	0.525
J0910.1-1816	J091003.9-181613	-3.586	1.934	3.166	3.662	5.474	1.872	4.113	-0.206	5.431	1.512
J0914.5+6845	J091429.10+684509	-8.271	2.549	6.052	5.26	7.978	2.189	19.984	-1.373	4.728	0.868
J0928.4-5256	J092818.7-525700	-3.339	2.918	3.417	4.01	5.963	3.388	12.625	-0.995	4.382	1.196
J0930.9-3030	J093058.0-303118	-4.275	1.466	3.227	4.036	5.655	1.015	23.599	-1.48	4.398	0.688
J0934.5+7223	J093334.0+722101	-4.41	1.826	5.781	4.019	7.194	2.513	8.466	-0.968	5.38	0.739
J0938.8+5155	J093835.0+515455	-5.437	2.839	3.725	4.268	5.67	2.986	10.506	-1.07	5.062	0.912
J1008.2-1000	J100749.3-094910	-4.962	4.0	7.004	4.427	6.438	3.376	20.832	-1.281	4.021	1.874
J1008.2-1000	J100802.5-095918	-4.843	2.725	2.847	3.665	5.353	1.82	17.248	-1.339	5.105	3.84
J1008.2-1000	J100848.6-095450	-5.284	1.604	6.832	3.82	7.237	3.687	27.338	-1.157	5.393	0.896
J1011.1-4420	J101132.0-442254	-6.402	3.016	2.26	3.773	6.028	1.82	14.274	-1.94	6.015	0.966
J1016.1-4247	J101620.8-424723	-6.032	2.157	5.036	4.565	5.472	3.937	19.153	-0.718	4.542	2.913
J1018.1-2705	J101750.2-270550	-5.168	2.491	6.696	4.418	5.52	2.652	15.713	-1.948	5.058	1.454
J1018.1-4051	J101801.5-405520	-1.512	1.182	2.8	2.469	5.589	2.733	7.348	-1.302	5.919	2.289
J1018.1-4051	J101807.6-404407	-4.582	3.5	2.999	3.852	5.564	3.072	9.331	-1.165	5.279	1.443
J1024.5-4543	J102432.6-454428	-3.666	3.996	2.903	3.92	5.62	3.39	19.133	-0.857	4.0	1.088
J1034.7-4645	J103438.7-464404	-4.961	3.999	3.419	4.138	7.008	3.71	18.373	-1.954	4.998	1.247
J1048.4-5030	J104824.2-502941	-6.609	3.969	2.101	4.197	5.342	3.732	19.891	-1.533	5.234	1.695
J1049.8+2741	J104938.8+274217	-3.408	2.054	2.673	3.39	5.453	2.146	16.0	-1.237	4.85	2.156
J1106.7+3623	J110636.7+362648	-3.553	2.085	6.715	4.226	7.973	1.042	17.753	-1.071	4.0	0.653
J1111.4+0137	J111114.2+013430	-4.444	3.997	3.518	3.979	7.116	3.7	12.205	-1.305	5.045	2.075
J1119.9-1007	J111948.2-100704	-5.732	2.518	3.82	4.419	5.71	2.409	18.917	-1.405	4.748	0.426

Table 3 continued

Table 3 (continued)

4FGL	XRT	$\log(k_e)$	p_1	p_2	$\log(\gamma_b)$	$\log(\gamma_{max})$	$\log(\gamma_{min})$	δ_D	$\log(B)$	$\log(t_{var})$	χ_r^2
									G	S	
J1122.0-0231	J112213.8-022916	-6.188	2.247	5.838	4.44	6.748	2.186	15.023	-1.415	5.242	1.175
J1146.0-0638	J114600.8-063850	-3.927	3.765	2.037	3.404	5.221	2.756	16.351	-1.369	4.915	2.015
J1155.2-1111	J115514.7-111125	-3.938	1.495	3.155	3.65	5.962	2.12	14.884	-1.671	5.162	1.249
J1220.1-2458	J122014.5-245949	-4.456	1.624	2.836	3.863	5.817	1.026	8.959	-1.008	5.266	0.384
J1243.7+1727	J124351.6+172643	-4.532	1.708	3.215	3.893	5.453	1.774	14.445	-1.153	4.926	1.112
J1256.8+5329	J125630.4+533203	-3.302	2.326	5.733	4.234	5.01	3.004	25.007	-1.996	4.037	1.448
J1326.0+3507	J132544.4+350450	-3.811	1.674	3.41	3.876	5.367	1.826	5.777	-0.476	5.217	0.998
J1326.0+3507	J132622.3+350627	-4.469	1.945	4.811	4.284	6.436	1.07	10.137	-0.68	4.63	0.283
J1415.9-1504	J141546.1-150228	-5.12	3.136	3.559	4.154	5.637	3.497	11.266	-0.859	4.965	0.847
J1429.8-0739	J142949.7-073302	-3.081	3.999	3.061	3.313	5.503	3.031	8.524	-0.646	5.218	3.172
J1513.0-3118	J151244.8-311648	-6.8	1.325	5.507	4.069	7.108	3.026	17.988	-0.553	5.619	1.963
J1514.8+4448	J151450.10+444957	-4.98	3.885	7.993	4.448	7.649	3.738	9.709	-0.692	4.56	1.512
J1528.4+2004	J152835.10+200423	-3.493	1.668	2.786	3.606	5.78	1.66	13.503	-1.183	4.712	0.99
J1545.0-6642	J154459.0-664147	-8.895	2.311	6.633	5.589	7.189	3.348	16.974	-1.375	4.98	1.635
J1557.2+3822	J155711.9+382032	-4.231	1.42	3.349	3.868	5.949	1.154	8.143	-1.209	5.317	0.892
J1631.8+4144	J163146.7+414634	-0.263	-0.574	2.384	2.0	5.422	2.708	22.615	-1.358	4.546	0.917
J1637.5+3005	J163728.2+300957	-4.399	2.4	3.218	3.732	5.821	2.813	15.826	-1.741	5.226	0.805
J1637.5+3005	J163739.3+301015	-2.613	2.326	4.503	3.58	6.627	3.41	13.662	-1.562	5.144	0.588
J1644.8+1850	J164457.3+185149	-5.648	2.594	4.877	4.482	5.242	2.789	18.771	-0.394	4.091	1.494
J1645.0+1654	J164500.0+165510	-4.693	2.03	3.486	4.106	5.898	2.192	41.146	-1.902	4.225	1.035
J1651.7-7241	J165151.5-724309	-6.914	2.801	3.412	4.64	5.832	2.541	16.39	-1.598	5.047	1.446
J1720.6-5144	J172032.7-514413	-4.116	3.983	3.053	3.75	6.059	3.453	14.546	-1.113	4.932	1.393
J1818.5+2533	J181830.9+253707	-3.025	-0.419	4.725	3.624	7.825	1.489	21.021	-0.516	4.362	0.592
J1846.9-0227	J184650.7-022903	-6.155	0.669	4.816	4.021	5.424	1.114	18.431	-1.222	5.976	2.013
J1910.8+2856	J191052.2+285624	-3.958	1.002	3.096	3.678	7.808	2.402	17.61	-1.999	5.27	1.542
J1910.8+2856	J191059.4+285635	-2.793	2.647	3.124	3.545	5.876	3.999	20.222	-1.971	4.862	1.225
J1918.0+0331	J191803.6+033030	-4.601	2.181	2.46	4.182	5.864	1.401	14.16	-1.692	4.755	2.079
J1927.5+0154	J192731.3+015356	-1.884	-1.766	2.513	2.668	5.572	2.491	15.004	-1.333	5.06	1.404
J1955.3-5032	J195512.5-503011	-4.586	2.697	4.135	4.178	7.901	2.898	7.503	-0.871	5.101	1.724
J2008.4+1619	J200827.6+161843	-2.876	1.72	3.207	3.649	5.695	1.606	18.052	-1.117	4.31	0.787

Table 3 continued

Table 3 (continued)

4FGL	XRT	$\log(k_e)$	p_1	p_2	$\log(\gamma_b)$	$\log(\gamma_{max})$	$\log(\gamma_{min})$	δ_D	$\log(B)$	$\log(t_{var})$	χ_r^2
									G	s	
J2041.1-6138	J204111.10-613952	-8.348	2.548	3.729	4.963	5.729	2.342	14.618	-1.717	5.639	1.263
J2046.9-5409	J204700.5-541246	-6.715	2.375	3.409	4.567	5.887	1.868	16.373	-1.769	5.256	0.725
J2109.6+3954	J210936.4+395513	-3.971	2.289	3.029	3.701	5.624	2.317	20.009	-1.454	4.659	3.829
J2114.9-3326	J211452.0-332532	-2.212	3.853	2.543	2.737	5.622	2.605	12.414	-1.218	5.293	1.088
J2159.6-4620	J215935.9-461954	-4.619	1.558	2.859	3.893	5.502	3.421	12.142	-1.137	5.141	1.038
J2207.1+2222	J220704.3+222234	-4.782	2.209	2.711	3.938	5.527	2.304	18.931	-1.544	4.838	0.79
J2222.9+1507	J222253.9+151052	-5.513	2.6	2.837	3.862	5.223	2.314	10.737	-0.87	5.47	0.431
J2225.8-0804	J222552.9-080415	-5.403	2.368	4.134	4.506	7.954	1.917	12.606	-0.924	4.577	1.148
J2237.2-6726	J223709.3-672614	-4.334	2.063	2.795	3.825	5.544	1.797	8.423	-0.865	5.183	0.572
J2240.3-5241	J224017.5-524117	-6.465	2.348	4.262	4.598	5.399	2.183	15.088	-1.169	5.055	0.757
J2247.7-5857	J224744.10-585500	-2.493	2.02	2.953	3.228	5.703	2.568	7.819	-1.047	5.29	1.75
J2303.9+5554	J230351.7+555618	-3.744	2.701	2.64	3.351	6.187	2.924	15.126	-2.0	5.437	2.605
J2311.6-4427	J231145.6-443220	-4.441	2.21	3.819	4.023	5.553	3.6	10.379	-0.815	4.93	0.82
J2317.7+2839	J231740.0+283954	-6.031	3.165	1.377	4.071	5.1	2.768	21.651	-1.284	4.82	0.725
J2326.9-4130	J232653.2-412713	-4.842	2.334	4.902	3.998	7.708	2.485	7.891	0.158	5.0	0.608
J2336.9-8427	J233627.1-842648	-6.009	3.76	2.174	4.586	5.317	3.478	10.276	-0.48	4.391	0.446
J2337.7-2903	J233730.2-290240	-0.815	2.583	2.611	2.375	5.141	2.087	8.092	-0.346	5.041	0.696
J2351.4-2818	J235136.5-282154	-6.182	2.059	4.489	4.059	5.468	2.12	21.662	-1.009	5.258	1.079